AHS Forum 73

Computational Aerodynamic Modeling of Small Quadcopter Vehicles

Seokkwan Yoon
NASA Advanced Supercomputing Division
NASA Ames Research Center
Moffett Field, California, U.S.A.

Patricia Ventura Diaz
STC
Moffett Field, California, U.S.A.

D. Douglas Boyd Jr.
Aeroacoustics Branch
NASA Langley Research Center
Hampton, Virginia, U.S.A.

William M. Chan
NASA Advanced Supercomputing Division
NASA Ames Research Center
Moffett Field, California, U.S.A.

Colin R. Theodore
Aeromechanics Office
NASA Ames Research Center
Moffett Field, California, U.S.A.

ABSTRACT

High-fidelity computational simulations have been performed which focus on rotor-fuselage and rotor-rotor aerodynamic interactions of small quad-rotor vehicle systems. The three-dimensional unsteady Navier-Stokes equations are solved on overset grids using high-order accurate schemes, dual-time stepping, low Mach number preconditioning, and hybrid turbulence modeling. Computational results for isolated rotors are shown to compare well with available experimental data. Computational results in hover reveal the differences between a conventional configuration where the rotors are mounted above the fuselage and an unconventional configuration where the rotors are mounted below the fuselage. Complex flow physics in forward flight is investigated. The goal of this work is to demonstrate that understanding of interactional aerodynamics can be an important factor in design decisions regarding rotor and fuselage placement for next-generation multi-rotor drones.

INTRODUCTION

Small multi-rotor vehicles have often been designed using an approach that consists of the steps "sketch, build, fly, and iterate". In that approach, there is no systematic way to explore trade-offs or determine logical next steps for design improvements. It is neither possible to account for multiple real-world constraints up front in design nor is it possible to know what the performance will be with a given design. Because unmanned vehicles are sized and optimized for particular missions, modern low-fidelity conceptual design and sizing tools that have been used for the design of large helicopters can also be used for the design of small multi-rotor craft. However, there are aerodynamic features of these multi-rotor vehicles that can be difficult to account for with these low-fidelity tools, unless there is a method to calibrate the tools.

Accurate prediction of rotorcraft performance continues to be challenging. The flows are inherently unsteady, nonlinear, and complex. A rotor blade can encounter its own tip vortex and the tip vortices of other blades. It is even more difficult when there are aerodynamic interactions between multiple rotors and fuselage because of the close proximity of all of these components. High-fidelity computational fluid dynamics (CFD) methods may offer an advantage over low-fidelity tools when investigations of interactional aerodynamics of multi-rotor vehicles are required. High-fidelity CFD can also provide information to calibrate low-fidelity design tools to account for aerodynamic interactions.

Small multi-rotor configurations often have low aerodynamic efficiencies both in hover and in cruise[1]. However, compared to single rotor systems, multi-rotor vehicles offer an advantage in lifting capacity[2] because the size of a single rotor is limited by the tip speed and structural mechanics.

The objective of the present work is to demonstrate a high-fidelity computational simulation capability to study the aerodynamics of complete multi-rotor systems both in hover and in forward flight. Two common quadcopters, DJI Phantom 3 and Straight Up Imaging (SUI) Endurance, are shown in Fig. 1. Simplified versions of these vehicle configurations are used in this study as representative vehicles in this small quadcopter class of vehicles. The simplified DJI configuration is used to examine the effects of different rotor vertical positioning (relative to the fuselage) on hover performance. The simplified SUI configuration includes rotors, fuselage, rotor mounting arms, and landing gear. This configuration is used to examine forward flight effects where fore and aft rotors operate at different RPM values.

DJI Phantom 3 SUI Endurance

Figure 1. DJI Phantom 3 and SUI Endurance Quadcopters

NUMERICAL APPROACH

In order to analyze aerodynamic performance and efficiency of small quadcopter vehicles, an overset grid approach, Chimera Grid Tools[3,4] for grid generation and OVERFLOW[5,6] for computational solutions, have been employed. OVERFLOW solves the Reynolds-Averaged Navier-Stokes (RANS) equations on structured overset grids. The current time-accurate approach consists of an inertial coordinate system where near-body (NB) curvilinear O-grids for the rotor blades and hub rotate through a fixed off-body (OB) Cartesian grid system.

Overset Grid Generation

The first vehicle for analysis in the present study is a simplified DJI Phantom 3 configuration. The DJI Phantom 3 simplified configuration consists of four rotors and a fuselage. The rotors are added to the fuselage in such way that there are two diagonally opposed rotors that rotate clockwise (CW) and the other two diagonally opposed rotors rotate counter-clockwise (CCW). The simplified fuselage for the aerodynamic study does not include landing gear, battery or camera.

Each rotor grid system consists of two blades and a hub. The rotor blades used for this study is Floureon's carbon-fiber (CF) replica of the 9443 rotor blades that are compatible with use on the Phantom 2 or Phantom 3. NASA Langley tested the CF replica rotor blades in the Structural Acoustic Loads and Transmission anechoic chamber facility[7]. The rotor blade geometric data were extracted from a high-resolution laser scan of the blade surfaces. Tests of Phantom 3 rotors at NASA Ames revealed that the original injection-molded flexible rotor blades yield higher performance and efficiency than the rigid CF rotor blades[8]. Nevertheless, the CF rotor blades are used in this study because the geometric information is already available. However, the geometry near the blades root has been slightly modified to have a narrow gap between the hub and rotor blades so that collective pitch angles can be changed. The CF rotor blade has a radius of 0.12m and a tip chord of 0.01m approximately. A grid system with 41 million grid points has been generated for an isolated rotor with a hub and two rotor blades. Each rotor blade consists of three near-body O-grids, one for the main rotor blade and two for the cap-grids for the inboard and outboard tips.

The fuselage surface of a Phantom 3 acquired by NASA Ames has been modeled using high-order polynomials and computer-aided design (CAD) software. A quadrotor system is constructed by incorporating multiple sets of the above-mentioned rotor grid system. Mirroring the CCW rotor generates the CW counterpart. The resulting near-body grids for four rotors and the fuselage consist of 74 overset grids. Off-body Cartesian grids with uniform spacing surround the rotor blades, hubs, and fuselage to resolve the wake region of interest. Coarser Cartesian grids efficiently expand the grid system to the far field, where each successive Cartesian grid is twice as coarse as its previous neighbor. The far-field boundary is 25 rotor radii away from the center of fuselage in all directions. The grid spacing normal to solid surfaces is chosen to maintain $y^+<1$. The resolved wake region has a uniform grid spacing of 10% of the tip chord length. The total number of grid points for a complete quadcopter with four rotors is approximately 225 million grid points. All surface and near-body volume grids in this study have been generated using Chimera Grid Tools. Domain connectivity has been performed using the X-rays approach in OVERFLOW.

Figure 2a shows a partial view of the surface grids of the simplified Phantom 3 quadcopter with four CF rotors.

The second vehicle employed in this study is the SUI Endurance quadcopter. The SUI quadcopter's original geometry has been slightly modified for the aerodynamic simulations, by removing, for example, the interior parts or the small pieces used to fold the arms, which do not change the main flow. The aerodynamic SUI configuration consists of the fuselage, four rotors, four arms, four motors, and landing gear. Again, the off-the-shelf rotors are added so that there are two diagonally opposed rotors that rotate CW and the other two diagonally opposed rotors rotate CCW.

Each rotor grid system consists of two blades joined together in the center, without a hub. The rotor blade geometry is the original T-Motor P15x5 CF blade. The geometric data were extracted from a high-resolution laser scan of the blade surfaces at NASA Ames. The T-Motor CF rotor blade has a radius of 0.19m and a tip chord of approximately 0.014m before the taper to the tip starts. A grid system with 49 million grid points has been generated for a single rotor with two rotor blades. Each rotor blade consists of two near-body O-grids, one for the main rotor blade and one for the cap-grid for the outboard tip.

The rest of the vehicle (fuselage, four arms, four motors, and landing gear) has been represented using a CAD model of the SUI quadcopter, provided by SUI to NASA Ames. The quadcopter is constructed by adding to the fuselage two fore arms and two aft arms, each arm supporting at its end the motor and the rotor blades. The fore and aft arms form an angle of 60 and 30 degrees with the fuselage longitudinal axis, respectively. The left fore blades, left aft blades, right aft blades and right fore blades (pilot view) rotate CW, CCW, CW and CCW, respectively. The landing gear is also added to the fuselage. The resulting near-body grids for the quadcopter consist of 176 overset grids. Off-body Cartesian grids with uniform spacing surround the rotor blades, fuselage, arms, motors, and landing gear to resolve the wake region of interest. Coarser Cartesian grids efficiently expand the grid system to the far field, where each successive Cartesian grid is twice as coarse as its previous neighbor. The far-field boundary is 25 rotor radii away from the center of the fuselage in all directions. The grid spacing normal to solid surfaces is chosen to maintain $y^+<1$. The resolved wake region has a uniform grid spacing of 10% of the tip chord length. The total number of grid points for the complete quadcopter is approximately 290 million grid points. Figure 2b shows a partial view of the surface grids of the SUI quadcopter.

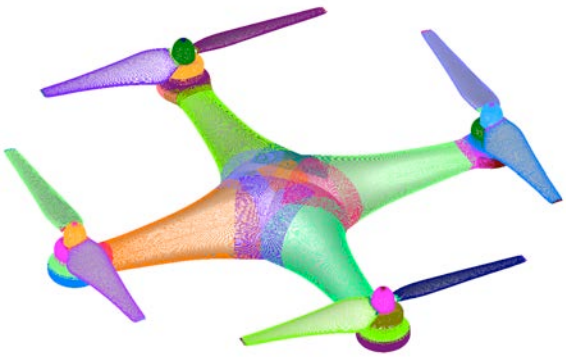

Figure 2a. Overset grids for the simplified DJI Phantom 3

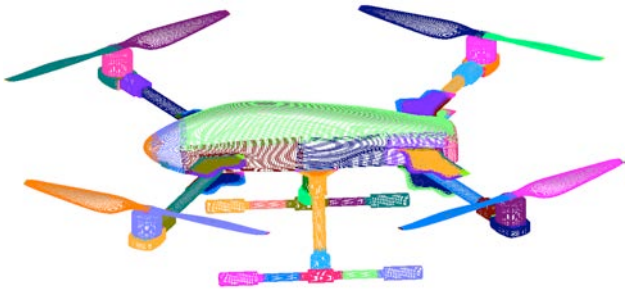

Figure 2b. Overset grids for the SUI Endurance

High-Order Accurate Navier-Stokes Solver

The Navier-Stokes equations can be solved using finite differences with a variety of numerical algorithms and turbulence models. In this study, the diagonal central difference algorithm is used with the 4th-order accurate spatial differencing option and matrix dissipation. Dual time-stepping is used to advance the simulation in time with 2nd-order time accuracy. The physical time step corresponds to 0.25 degrees rotor rotation, together with up to 50 dual-time sub-iterations for a 2.5 – 3.0 orders of magnitude drop in sub-iteration residual. This numerical approach and time step was previously validated for various rotor flows.[9-12] In order to reduce the computational time required for a converged solution, the first 1440 steps employ a time step of 2.5 deg, yielding 10 rotor revolutions. The time step is then reduced to 0.25 deg, for which 1440 steps correspond to one rotor revolution.

Low Mach Number Preconditioning

One of the challenges for compressible Navier-Stokes methods in computing small-rotor flows is the relatively low Mach number flow due to small rotor radii. For example, in the case of the DJI Phantom, the Mach number at the tip of blades is under 0.2 at 5,400 RPM. Mach numbers at the inboard locations are obviously even lower. Compressible Navier-Stokes codes in general suffer from slow convergence for low speed flows because of a disparity between the acoustic and convective speeds. Because most numerical algorithms have a stability restriction on the size of the time step determined by the maximum eigenvalue, the acoustic speed limits the time step. On the other hand, convergence to a steady state is controlled by the convective speed, which determines how fast low-frequency errors are advected out of the computational domain. If the convective speed is much smaller than the speed of sound, the stability restriction forces time steps so small that convergence requires a large number of iterations. Low Mach number preconditioning[13,14] is an attempt to equilibrate the eigenvalues, making them all of the same order of magnitude and thus decreasing the number of iterations to convergence. Low Mach number preconditioning is only used during the sub-iteration steps at each physical time step.

Hybrid Turbulence Modeling

Rotorcraft simulations using the Detached Eddy Simulation[15] (DES) model have been successfully performed to predict the Figure of Merit (FM) accurately. The RANS equations require a closure by modeling the Reynolds stress. The one-equation Spalart-Allmaras[16] (SA) RANS model is one of the models commonly used to compute the turbulent eddy viscosity using the Boussinesq approximation to relate the Reynolds stresses to a kinematic turbulent eddy viscosity and the mean strain-rate tensor. The turbulence length scale, d, is defined as the distance from a field point to the nearest wall. The accuracy of the SA-RANS model depends strongly on the source terms, which were primarily developed for attached boundary-layer flows along flat plates, wings, fuselages, etc.

The turbulence length scale, d, plays a key role in accurately determining the rotor FM. A problem occurs deep within the rotor wake, where d may be several rotor radii in length. In this case, d no longer represents an estimate of the largest turbulent eddy in the local flow, but rather a very large geometric parameter. When d is very large the turbulence dissipation becomes very small. On the other hand, the strong tip vortices in the lower wake can generate significant turbulence production. Over time, this imbalance in turbulence production and dissipation in the lower wake can result in excessively large eddy viscosities. These large viscosities can migrate up the vortex wake after several rotor revolutions and, under blade-vortex interaction conditions, infiltrate the blade boundary layers. When this happens, the rotor blade drag and torque increase significantly and artificially, resulting in large FM errors and an under-prediction of rotor efficiency.

The DES model is a RANS/LES hybrid approach that mitigates the problem of artificially large eddy viscosity. The turbulence length scale is modified by replacing the minimum of the distance from the wall with the local grid spacing. This simple but crucial change can be viewed in two different ways. From a numerical perspective the length scale has been significantly reduced. This allows the turbulence dissipation to remain active in the vortex wake below the rotor plane and prevents the turbulent eddy viscosity from growing to unrealistic values. The torque therefore remains unaffected, compared to the process described above, and the FM is accurately predicted. A physical interpretation views the modified length scale as an implicit filter, where the largest turbulent eddies are now grid-resolved. All smaller eddies are modeled by a reduced turbulent eddy viscosity. This DES approach provides a rational way to reduce the length scale, and hence the turbulent eddy viscosity, based on a physical model.

The DES approach assumes that the wall-parallel grid spacing exceeds the thickness of the boundary layer so that the RANS model remains active near solid surfaces. If the wall-parallel grid spacing is smaller than the boundary layer thickness, then the DES Reynolds stresses can become under-resolved within the boundary layer, and this may lead to non-physical results, including grid-induced separation. Using Delayed Detached Eddy Simulation[17] (DDES), the RANS mode is prolonged and is fully active within the boundary layer. The wall-parallel grid spacing used in this study does not violate the hybrid-LES validity condition. Thus DES and DDES should give similar results. Nevertheless, all computations have been performed using the DDES model for both NB and OB grids.

Supercomputer

All computations have been performed on Pleiades supercomputer at the NASA Advanced Supercomputing Division using Intel 28-core Broadwell nodes. It takes about 10-14 hours for 30 revolutions on 1024 cores for isolated rotor simulations and 48-72 hours for quadcopter vehicles.

RESULTS

Isolated Rotors

First, a single CF rotor for the DJI Phantom in hover has been simulated for a wide range RPM. Vorticity magnitude contours are compared in Fig. 3 for 3600, 5400, and 7200 RPM. The tip Mach number and Reynolds number, however, are different for each case due to the differences in RPM.

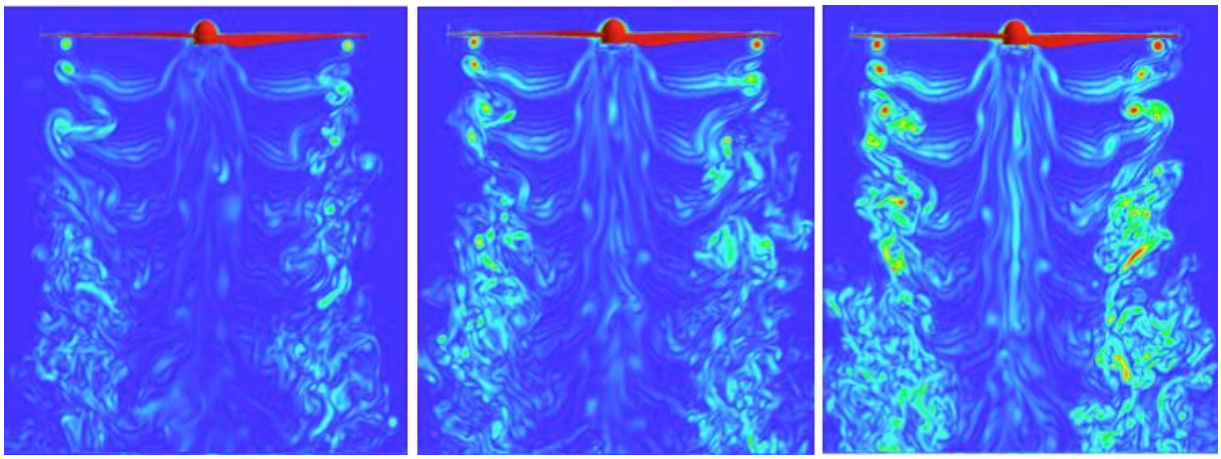

3600 RPM 5400 RPM 7200 RPM

Figure 3. Vorticity magnitude for the DJI Phantom CF rotor at various RPMs (3600, 5400, and 7200); 0 deg pitch

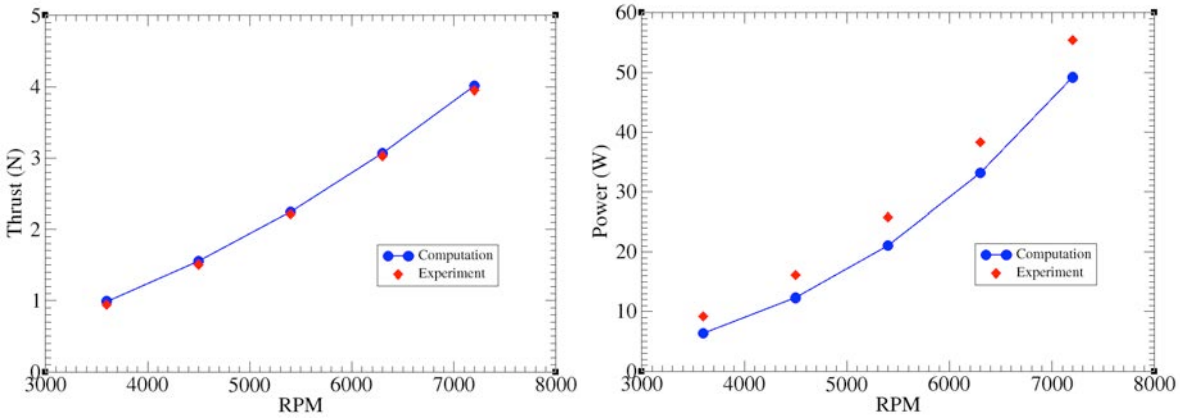

Figure 4. Comparison with Zawodny's experimental data for the DJI Phantom CF rotor at various RPMs (3600, 4500, 5400, 6300 and 7200)

A comparison of computational results with the experimental data[7] in Fig. 4 for 3600, 4500, 5400, 6300, and 7200 RPM shows excellent agreement for the thrust and a linearly increasing difference for power. Whereas the measured power is for both the rotor and motor, the computed power is only due to rotor aerodynamics. Considering that the electrical power loss for the motor increases linearly with RPM, the agreement in trend for power is very good also.

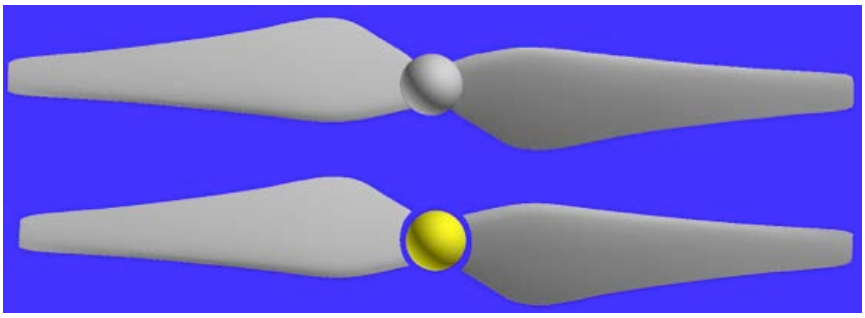

Figure 5. Modification of the DJI Phantom CF rotor to change collectives (upper: original, lower: modified). Note a narrow gap between the hub and blades in the modified rotor.

In order to study the effects of collective pitch on the performance, a narrow space between the hub and rotor blades has been created as shown in Fig. 5. The gap space has been carefully designed so that it is wide enough to change pitch angles up to 20 deg. but narrow enough not to affect flow characteristics. The pitch angle for the baseline rotor blade is 0 deg. Velocity magnitude contours for 0, 4, and 8 deg. of pitch at 5400 RPM are shown in Fig. 6. High downwash speeds indicated by red suggest increases in thrust. Figure 7 shows the thrust and torque trends at various collectives varying from 0 to 12 deg. in increments of 2 deg. Because the increase in thrust is linear while the torque increase is quadratic, the FM peaks at the 8 deg. pitch as shown in Fig. 8a. As RPM increases, torque increases more rapidly than thrust. Figure 8b shows collective pitch angles for equivalent thrust. For example, 3.5 deg. pitch at 5400 RPM or 8.5 deg. pitch at 4500 RPM can generate the same level of thrust as 0 deg. pitch at 6300 RPM. Because the trend line is almost linear, it may be possible to use interpolation to find the pitch angle at other RPMs. Lower RPMs for equivalent thrust may lead to lower noise.

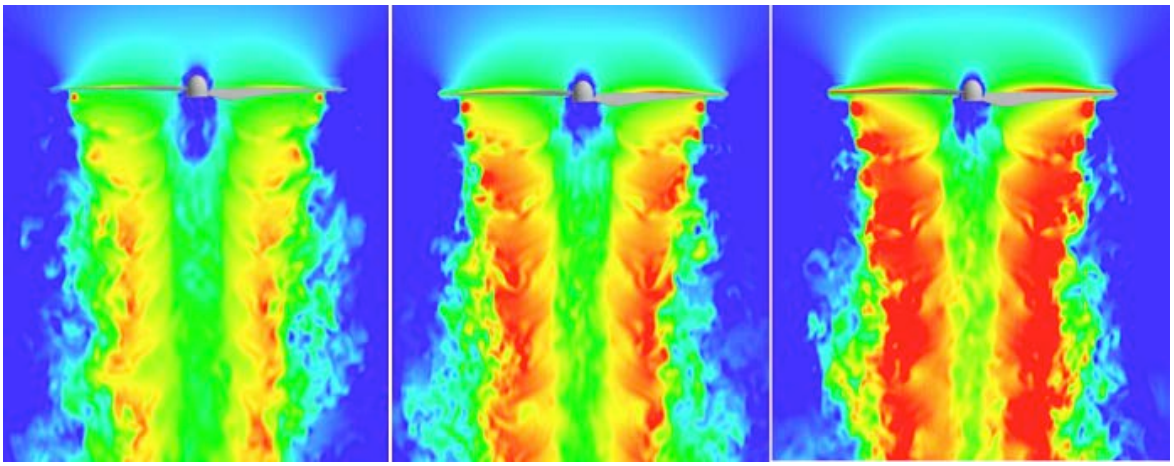

Figure 6. Velocity magnitude for the DJI Phantom CF rotor at various collectives (0, 4, and 8 deg); 5400 RPM

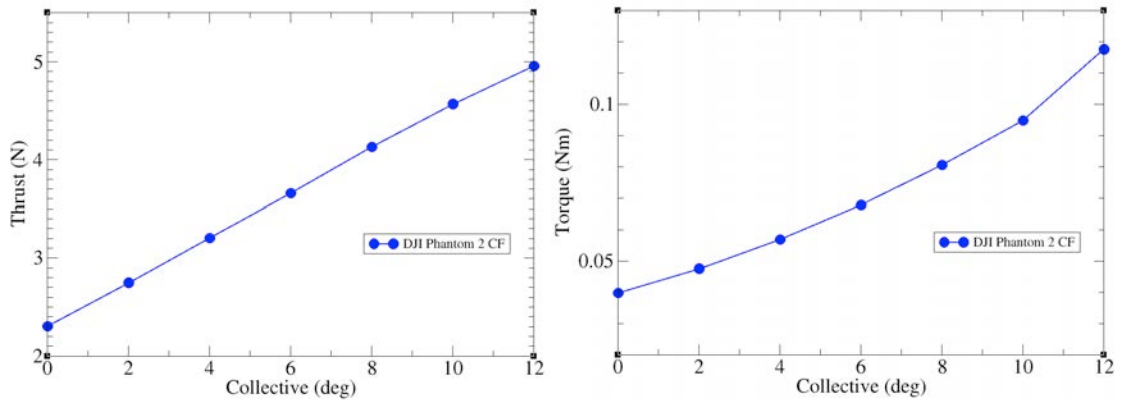

Figure 7. Thrust and torque trends for the DJI Phantom CF rotor at various collectives (0 – 12 deg with an interval of 2 deg)

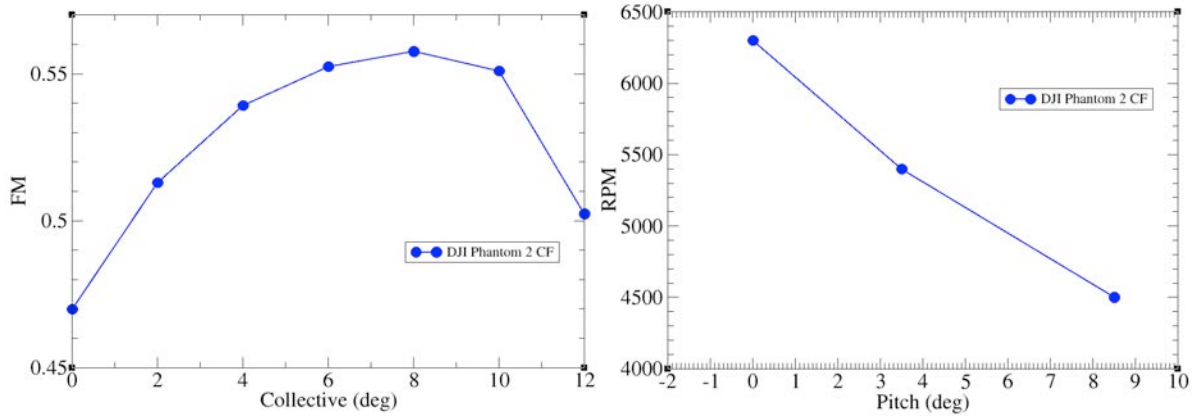

(a) FM vs. collective (b) Collective pitch angles for equivalent thrust

Figure 8. (a) FM trend and (b) Equivalent collective and RPM for given thrust for the DJI Phantom CF rotor

For comparison with the CF rotor blades, NASA Ames scanned the Phantom 3 factory plastic blades. Figure 9 shows a comparison of blade characteristics between the CF and factory blades. Chord length is normalized by the rotor radius. A clear difference between two blades is the twist angle. The Phantom 3 blade has much higher twist than the CF blade. At outboard radial stations where most thrust is generated, the difference in twist is approximately 4 deg. That is why the pitch is adjusted to 4 deg. in our DJI quadcopter simulations using the CF rotors. Moreover, probably due to the manufacturing process, the airfoil shapes of the CF blade near the rotor tip are more like thick flat plates than airfoils. Therefore, the Phantom 3 plastic blades generate higher thrust than the CF blades at 4 deg. pitch.

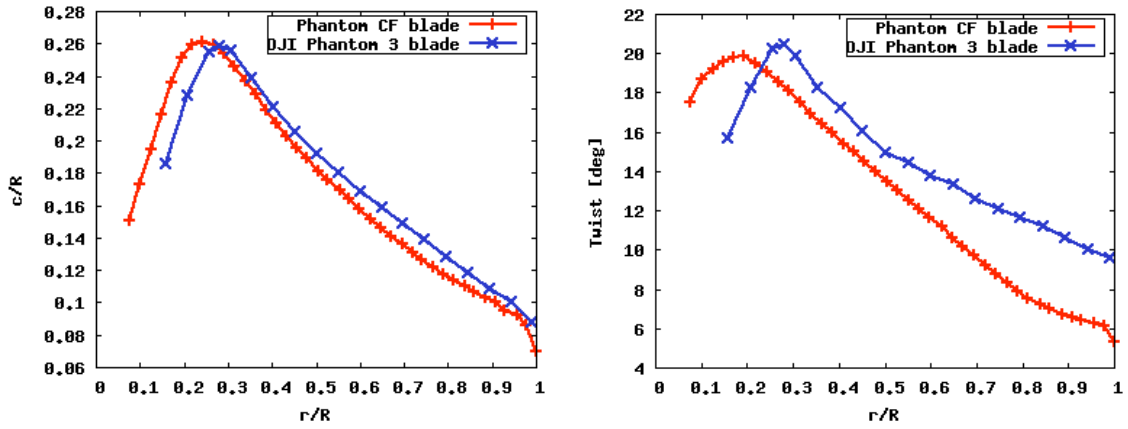

Chord Twist

Figure 9. Comparison of DJI Phantom 3 plastic and CF blades (normalized by the rotor radius)

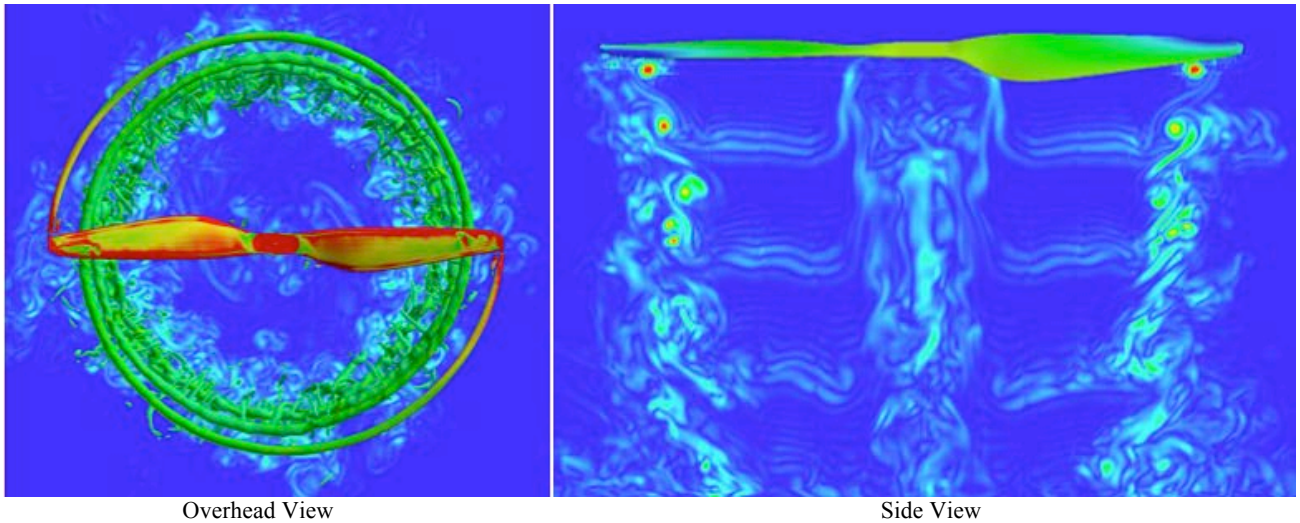

Overhead View Side View

Figure 10. Vorticity for the SUI Endurance rotor in hover at 3500 RPM

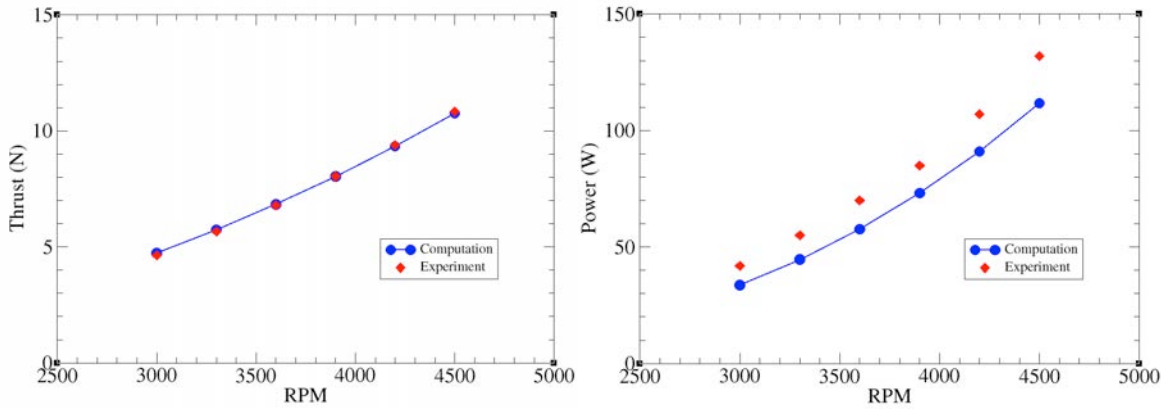

Thrust vs. RPM Power vs. RPM

Figure 11. Comparison with Zawodny's experimental data for the SUI Endurance rotor at various RPMs (3000, 3300, 3600, 3900, 4200 and 4500)

Figure 10 shows vorticity magnitude contours for the SUI Endurance rotor in hover at 3500 RPM. The tip Mach number and the Reynolds number for the 3500 RPM case are 0.2 and 65716 respectively. This rotor is comprised of two rotor blades joined together in the center of the rotor and therefore does not have a traditional hub structure. The flow-fields below the rotor center look slightly different from conventional rotors. A comparison of computational results with the experimental data[7] in Fig. 11 for 3000, 3300, 3600, 3900, 4200, and 4500 RPM shows excellent agreement for the thrust and a linearly increasing difference for power. Whereas the measured power is for both the rotor and motor, the computed power is only due to rotor aerodynamics. Considering that the electrical power loss for the motor increases linearly with RPM, the agreement in trend for power is very good also.

DJI Phantom 3

The first solution of the simplified DJI Phantom 3 was obtained in a previous study[2] of its coaxial rotor variant. An accompanying video was posted on the NASA website[a] as well as on several NASA social media platforms including Facebook[b] and YouTube[c]. It was also featured on many magazines including Wired[d], Cosmos[e], ECN[f] and Digital Trends[g]. The video revealed the dynamic and intricate interactions between multiple rotors and the airframe. In this configuration, the rotors are mounted above the fuselage (called the "overmount rotors" here). When the overmount rotors pass over the fuselage arms, the fuselage experiences a download from the rotor aerodynamics. The rotor-arm interaction is also the source of thrust oscillations that can decrease the stability of the vehicle. The electronic flight control system is used to stabilize the vehicle, but at the expense of reduced battery life and flight time.

In this study, an unconventional configuration is also examined. In this unconventional configuration, the rotors are placed on the underside of the fuselage arms instead of above. Two different rotor locations are examined for this unconventional configuration. In the first (the "undermount"), the rotors are the same distance below the arms as the conventional rotors are above the arms. In the second (the "off-body undermount"), the rotors are at a distance of a quarter of the rotor radius below the hub in this example. It should be noted that the undermount would not be possible with the real Phantom 3 because landing gear and other parts would interfere with the rotors.

Figure 12 shows iso-surfaces of the instantaneous Q-criterion and pressure for three configurations: the original with overmount rotors, one with undermount rotors, and one with off-body undermount rotors. Rotor positions are not in phase.

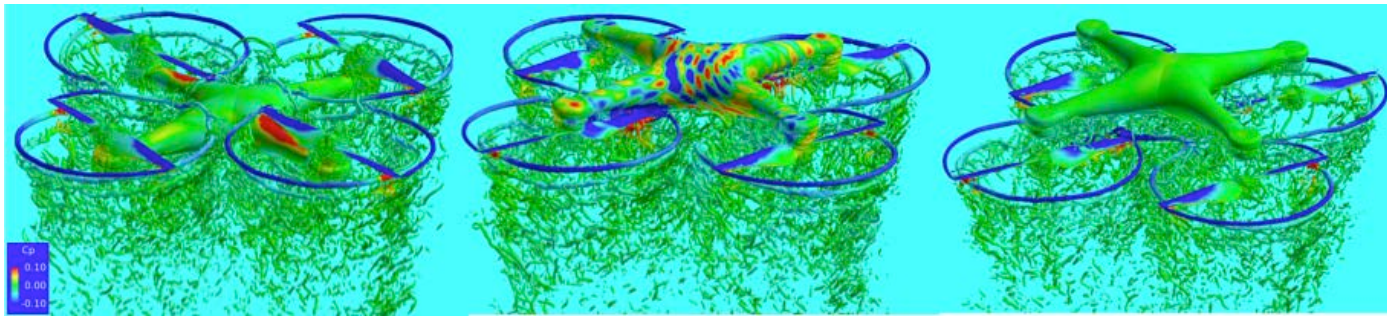

Overmount Undermount Off-body Undermount

Figure 12. Iso-surfaces of Q-criterion for Overmount, Undermount, and Off-body Undermount rotors; Pressure shown at the body surface.

[a] https://www.nasa.gov/image-feature/ames/exploring-drone-aerodynamics-with-computers
[b] https://www.facebook.com/nasaames/videos/vb.338122981393/10153991840876394/?type=2&theater
[c] https://www.youtube.com/watch?v=hywBEaGiO4k
[d] https://www.wired.com/2017/01/stunning-animation-reveals-air-swirling-around-drone/
[e] https://cosmosmagazine.com/physics/drone-aerodynamics
[f] https://www.ecnmag.com/blog/2017/01/nasa-reveals-drone-aerodynamics-supercomputers
[g] http://www.digitaltrends.com/cool-tech/nasa-double-the0thrust-dji-simulation/

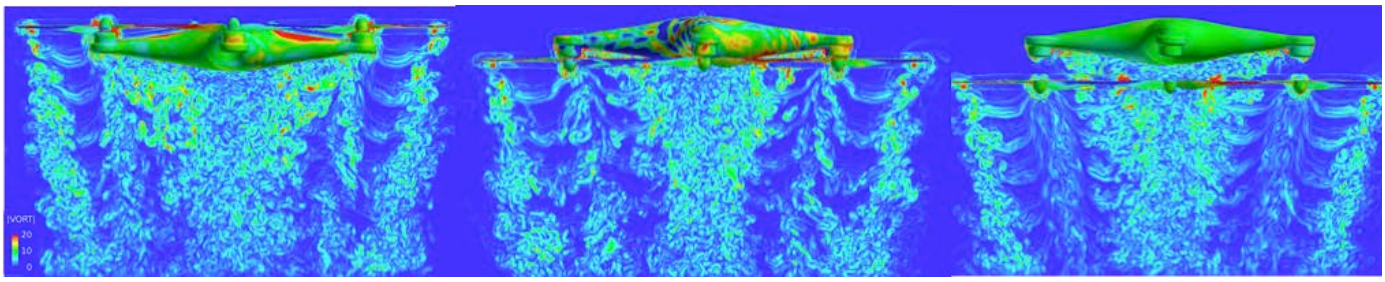

Overmount Undermount Off-body Undermount

Figure 13. Vorticity magnitude for Overmount, Undermount, and Off-body Undermount rotors; Pressure shown at the body surface.

Figure 13 shows a comparison of vorticity magnitude in the wake. While the overmount configuration exhibits strong interactions between the inboard rotor wake and the fuselage wake, the off-body undermount configuration appears to have significantly more rotor-rotor interactions. Figures 14 and 15 show pressure for upper and lower surfaces respectively. The pressure distribution on the fuselage of the undermount configuration appears to be much more unsteady than that seen on the overmount or off-body undermount configurations.

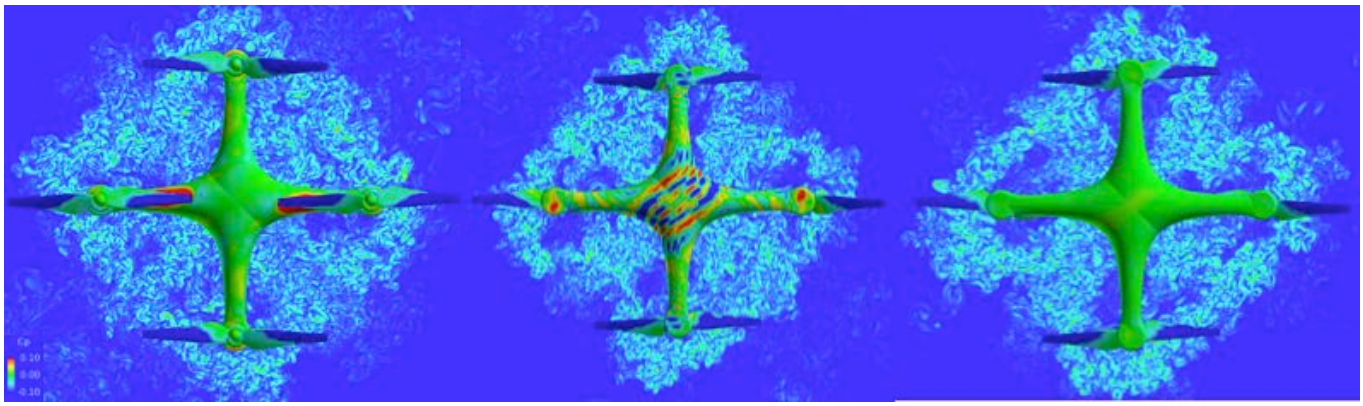

Overmount Undermount Off-body Undermount

Figure 14. Surface pressure for Overmount, Undermount, and Off-body Undermount rotors (upper surface); Vorticity shown at a plane below the vehicle.

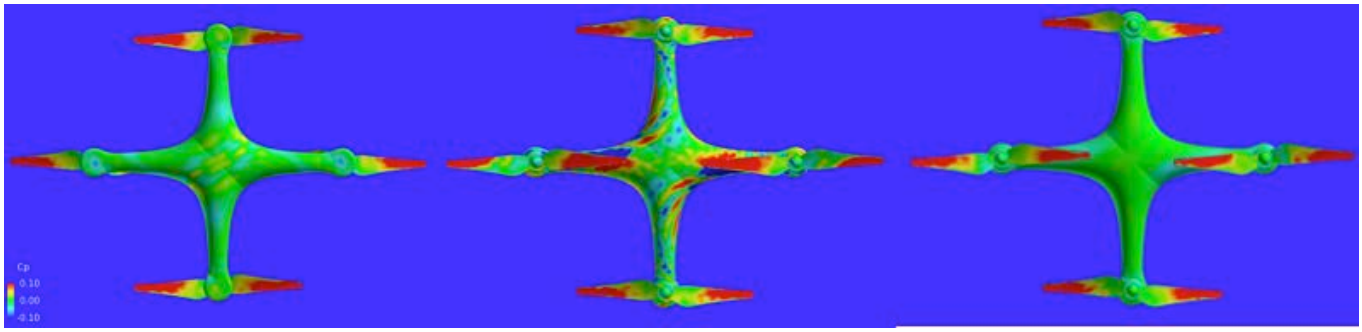

Overmount Undermount Off-body Undermount

Figure 15. Surface pressure for Overmount, Undermount, and Off-body Undermount rotors (lower surface)

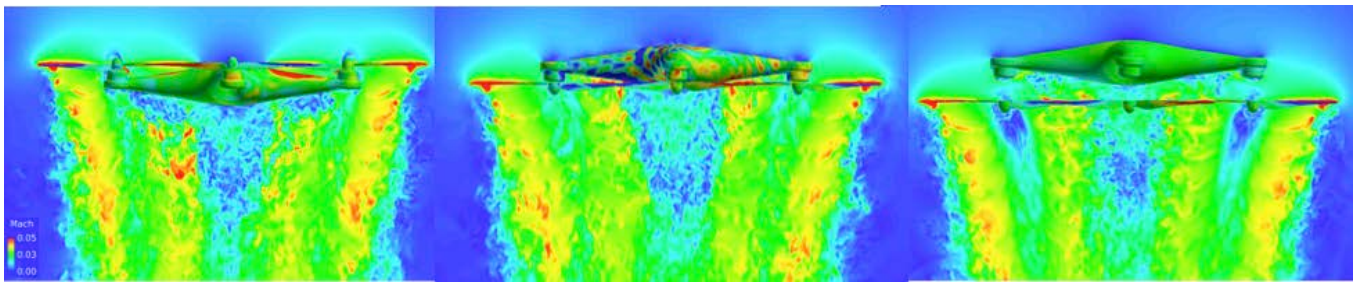

Overmount Undermount Off-body Undermount

Figure 16. Velocity magnitude for Overmount, Undermount, and Off-body Undermount rotors; Pressure shown on the surface.

Figure 16 shows a comparison of velocity magnitude. Red indicates high speeds. The overmount configuration exhibits highest speed downwash of the three configurations from the inboard rotor blades; whereas the off-body undermount configuration exhibits the lowest. Table 1 shows that the undermount configuration generates 1 percent less total thrust than the overmount, and the off-body undermount configuration generates 2 percent less than the undermount configuration. Figure 17 shows pressure on a vertical plane through the center of the vehicle. While the high pressure below the overmount rotors pushes down the fuselage, the low pressure above the undermount rotors pulls down the fuselage by almost the same force as the overmount configuration. Compared to the undermount configuration, the fuselage of the off-body undermount configuration experiences much less download. However, without significant interference from the fuselage, four rotors experience strong interactions between themselves. Note smaller red zones below the inboard rotor blades for the off-body undermount. A previous study[11] indicates that as the separation distance between rotors deceases, the total thrust of quadrotors also decreases. The thrust only from rotors for the off-body undermount is 6 percent less than the undermount and 7 percent less than the overmount. Figure 18 shows a comparison of downwash between a quadrotor and an octorotor. Rotor positions are in phase. Mounting rotors both above and below arms can increase the thrust significantly.

Configuration	Rotor Thrust	Fuselage Download	Total Thrust
Overmount	1.025	-0.076	0.949
Undermount	1.016	-0.080	0.936
Off-body Undermount	0.954	-0.038	0.916

Table 1. Total thrust for various quadrotor configurations (Forces have been normalized by 4x an isolated single rotor thrust.)

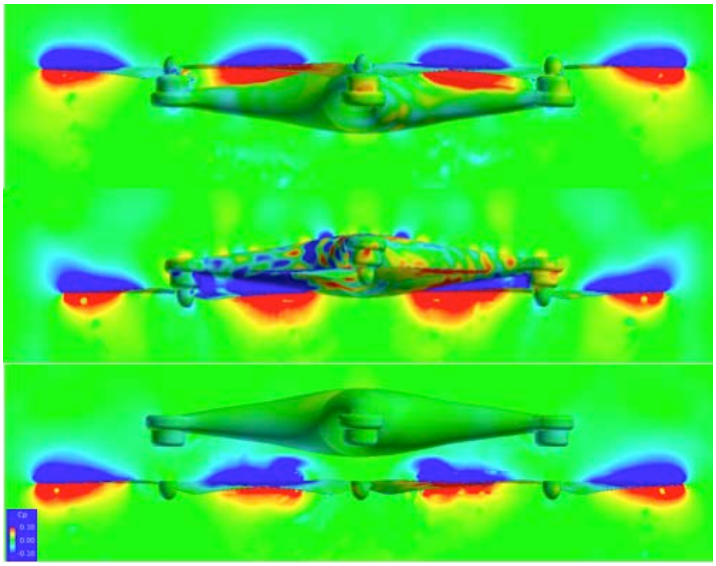

Figure 17. Pressure for Overmount (top), Undermount (middle), and Off-body Undermount (bottom) rotors

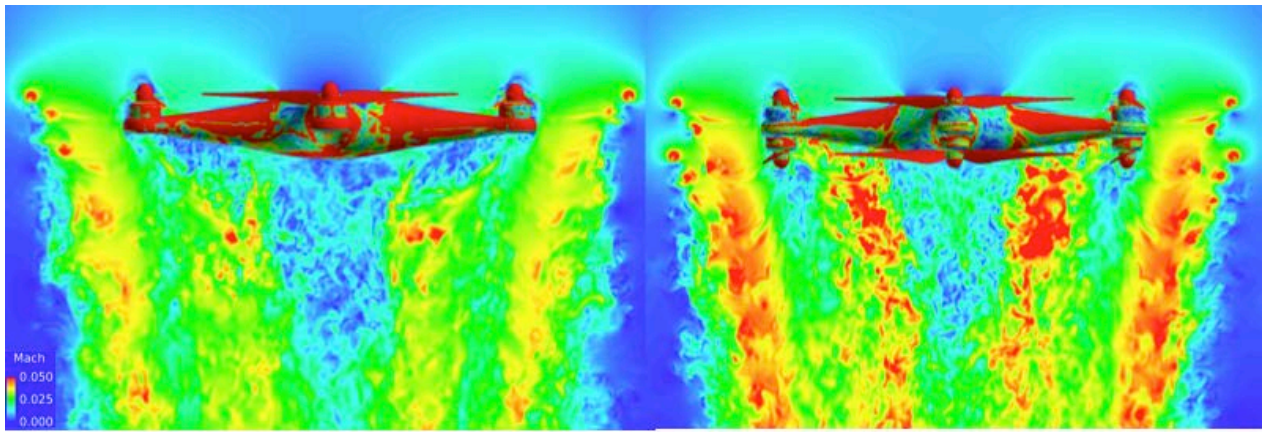

Quadrotor Coaxial Quadrotor

Figure 18. Downward velocitiy magnitude for an overmount quadrotor and a coaxial quadrotor (octorotor); Rotor positions are in phase.; Vorticity shown at the body surface.

SUI Endurance

Recently, both flight tests and wind tunnel experiments were conducted for the SUI Endurance. Preliminary results have been obtained for selected test conditions. The SUI Endurance configuration includes four rotors, fuselage, arms, canards, motors, payload mount rails, and landing gear. Figures 19 and 20 show the iso-surfaces of the Q-criterion and surface pressure at 3500 RPM in hover. The tip Mach number and the Reynolds number for this case are 0.2 and 65716, respectively. With relatively large separation distances between rotors, the rotor-rotor interactions are smaller than those for the DJI configuration. Aside from flat canards, thin arms limit download and thrust oscillations. Clearly, this configuration appears to be a better design for hover than conventional quadcopters in terms of the reduced negative interaction between the rotors due to their large separation distances.

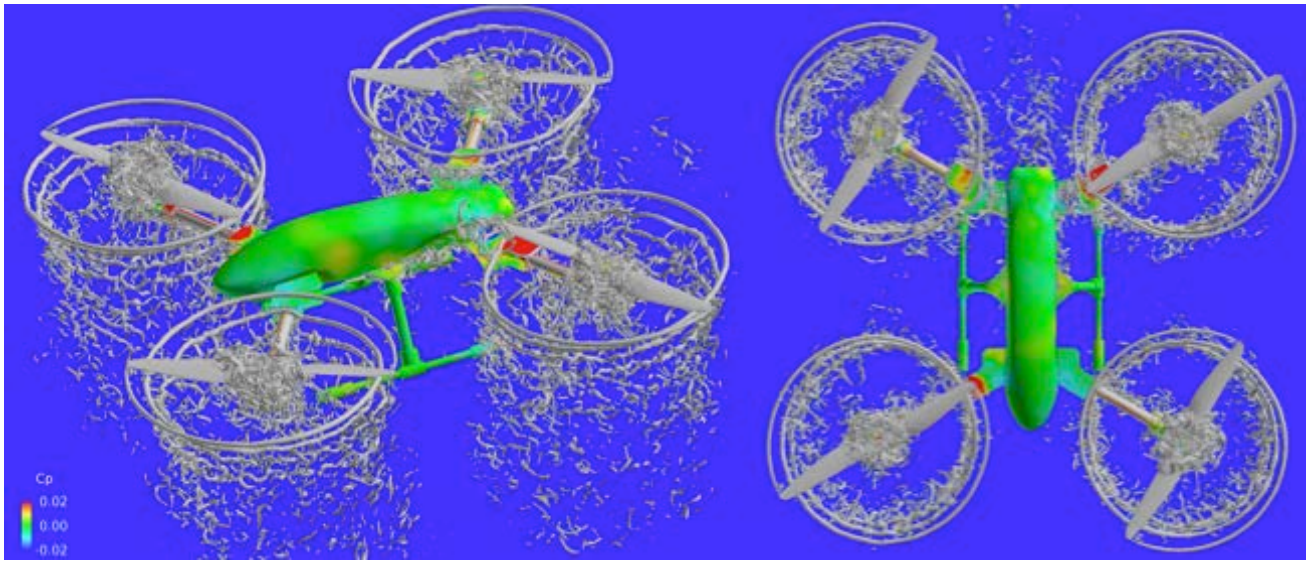

Oblique View Overhead View

Figure 19. Iso-surfaces of Q-criterion and surface pressure for the SUI Endurance in hover (3500 RPM)

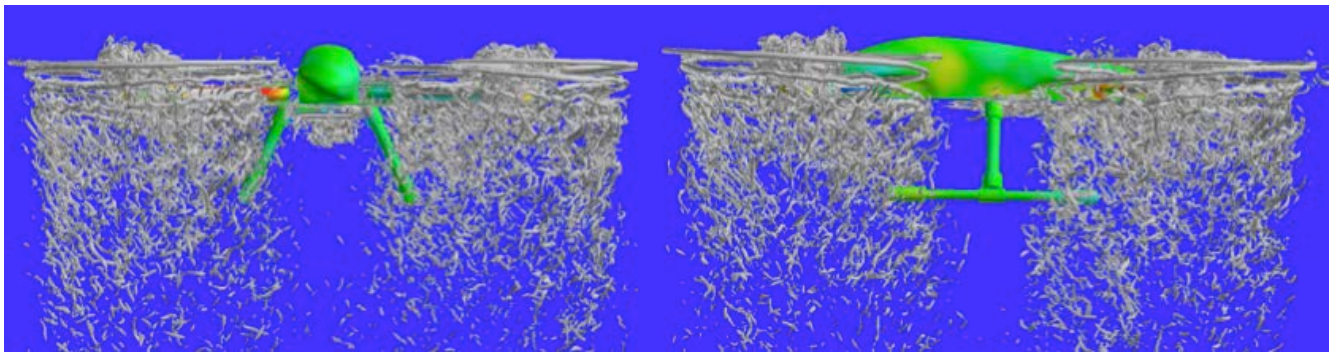

Front View Side View

Figure 20. Iso-surfaces of Q-criterion and surface pressure for the SUI Endurance in hover (3500 RPM)

Two forward flight conditions have been simulated. Conditions for trim were measured in flight tests. Fore and aft rotors rotate at different RPMs and hence have different periods. The present study represents the first high-fidelity CFD simulations for quadrotors where the rotors are at different rotational speeds. Rotor positions are not in phase. Figures 21 and 22 show the flows at 5 m/sec (11.18 mph or Mach 0.0146) and -3.4 deg. angle of attack. RPMs for the fore and aft rotors are 3660 and 4350, respectively. The aft rotors rotate 18.9 percent faster than the fore rotors. The advance ratio based on the fore rotors is 0.0685. Rotor-rotor interactions increase as the wakes of the fore rotors begin to affect those of the aft rotors. Formation of supertip vortices from the fore rotors is visible. There are significant blade-vortex interactions in the fore rotors. The aft rotors generate approximately 23 percent higher thrust than the fore rotors (as compared to 41 percent for an isolated rotor).

Figures 23 and 24 show the flows at 10 m/sec (22.37 mph or Mach 0.0292) and -7.7 deg. angle of attack. RPMs for the fore and the aft rotors are 3510 and 4410, respectively. The aft rotors rotate 25.6 percent faster than the fore rotors. The advance ratio based on the fore rotors is 0.1429. Rotor-rotor interactions are strong as the wakes of the fore rotors merge into those of the aft rotors. Supertip vortices from both fore and aft rotors are visible. The inboard supertip vortices from the fore rotors interact with the fuselage and then are fed into the advancing side of the aft rotors near the juncture of the fuselage and the aft canards. There are some blade-vortex interactions in the fore rotors. The aft rotors generate approximately 30 percent higher thrust than the fore rotors (as compared to 58 percent for an isolated rotor). Because the results from this configuration are preliminary, comparison of these results to experimental data is left to future work.

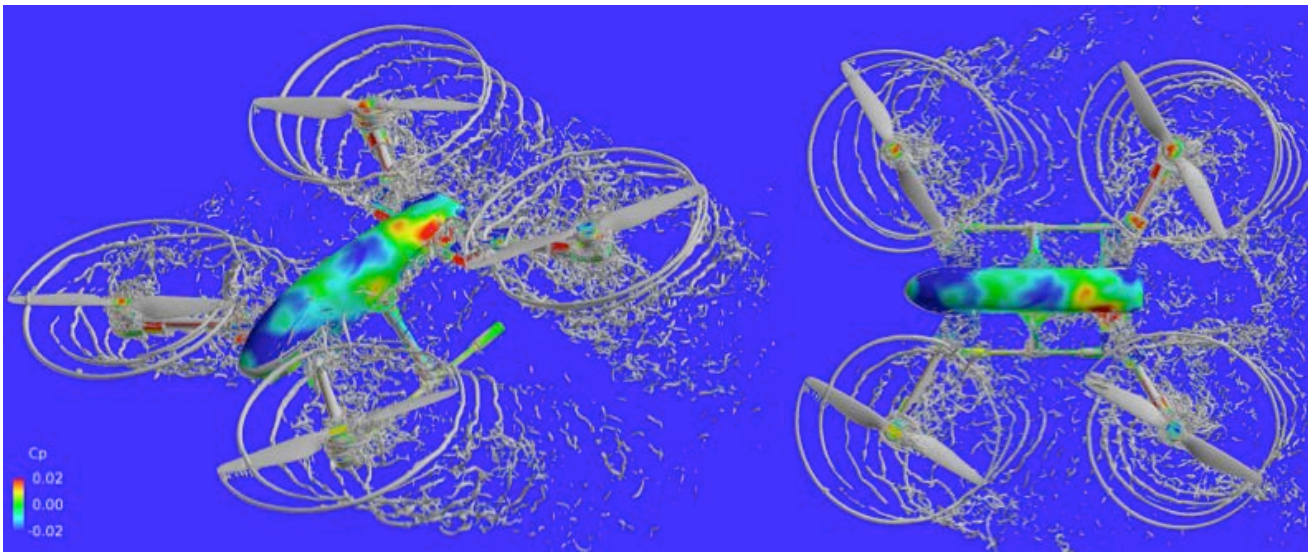

Oblique View Overhead View

Figure 21. Iso-surfaces of Q-criterion and surface pressure for the SUI Endurance in forward flight (freestream velocity 5m/sec or Mach 0.0146, angle of attack -3.4 deg, fore rotor RPM 3660, aft rotor RPM 4350, Advance Ratio 0.0685)

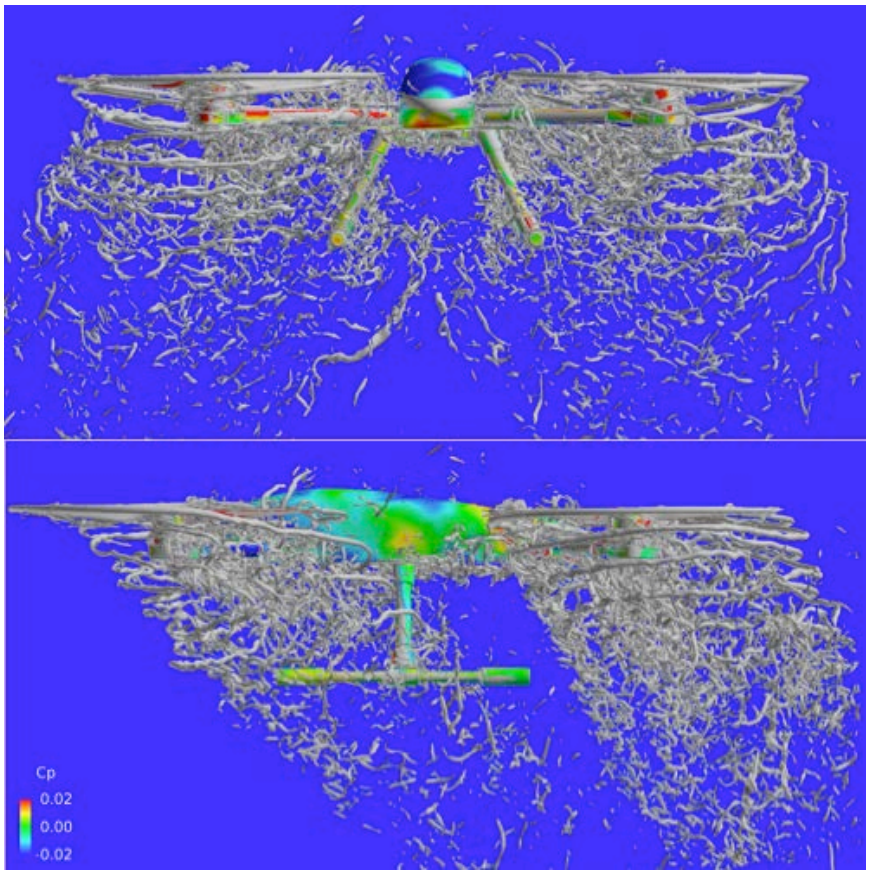

Figure 22. Iso-surfaces of Q-criterion and surface pressure for the SUI Endurance in forward flight (freestream velocity 5m/sec or Mach 0.0146, angle of attack -3.4 deg, fore rotor RPM 3660, aft rotor RPM 4350, Advance Ratio 0.0685); front and side views.

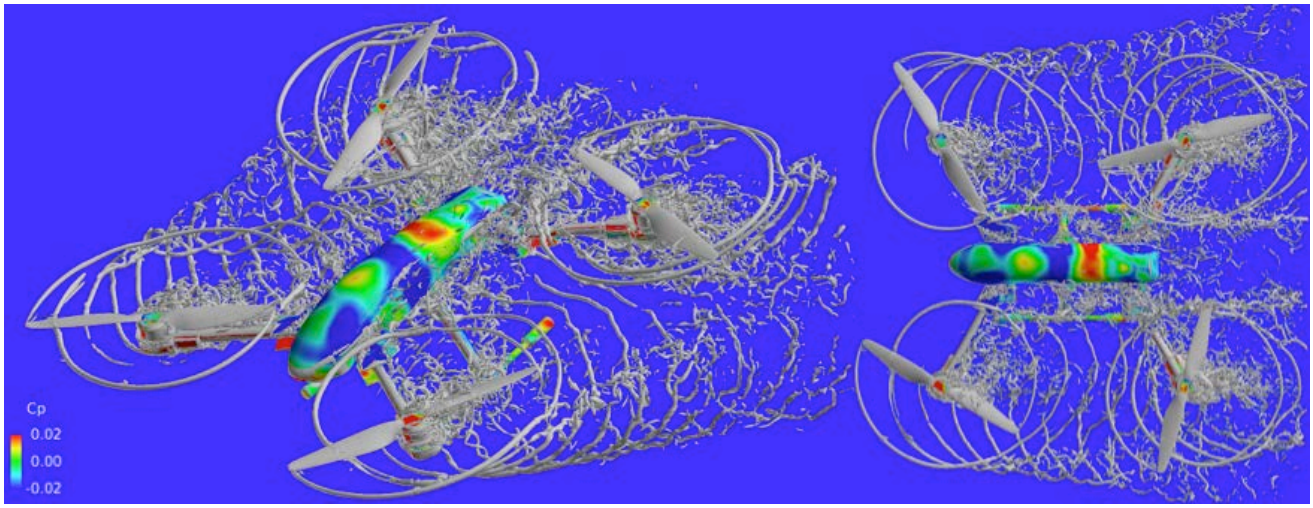

Oblique View Overhead View

Figure 23. Iso-surfaces of Q-criterion and surface pressure for the SUI Endurance in forward flight (freestream velocity 10m/sec or Mach 0.0292, angle of attack -7.7 deg, fore rotor RPM 3510, aft rotor RPM 4410, Advance Ratio 0.1429)

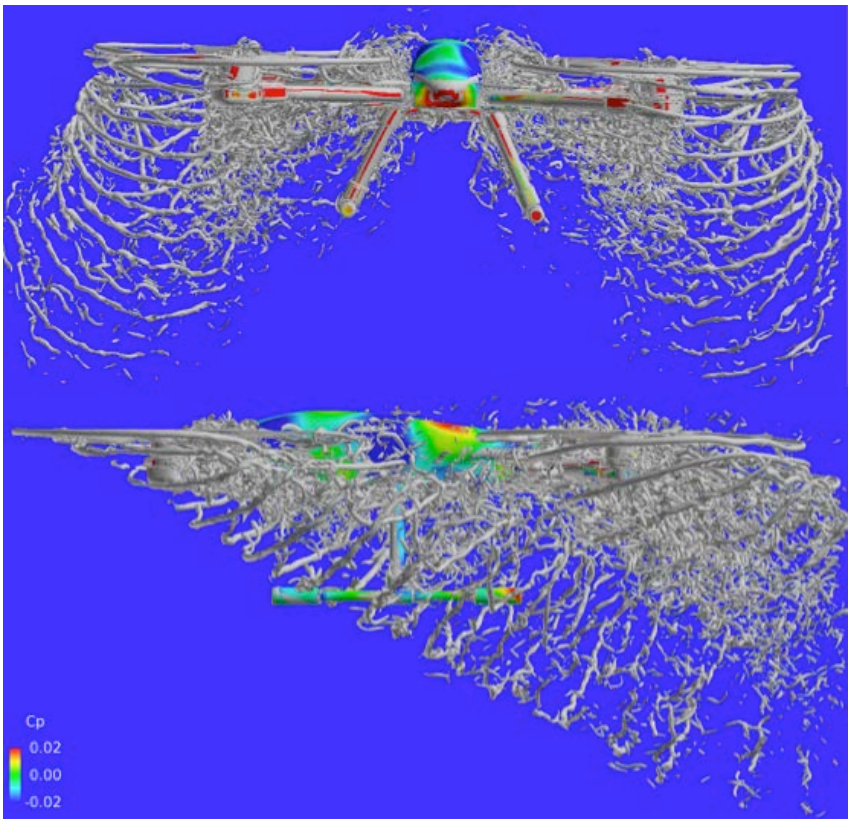

Figure 24. Iso-surfaces of Q-criterion and surface pressure for the SUI Endurance in forward flight (freestream velocity 10m/sec or Mach 0.0292, angle of attack -7.7 deg, fore rotor RPM 3510, aft rotor RPM 4410, Advance Ratio 0.1429); front and side views.

SUMMARY

A high-fidelity computational simulation capability has been demonstrated for interactional aerodynamic modeling of two representative, small quad-rotor vehicle systems. Computational results for isolated rotors show excellent agreement with the available experimental data. The configuration with undermount rotors does not offer any improved performance compared to the traditional configuration with overmount rotors. Strong pressure waves seen on the surface of the configuration with undermounted rotors suggest a highly unsteady aerodynamic environment on the fuselage. The off-body undermount rotors generate lower thrust than the undermount rotors. A configuration that has large separation between the rotors appears to be an efficient design for hover. Forward flight tends to result in aerodynamic interactions between the fore and aft rotors, which decreases the efficiency of the aft rotors. High-fidelity CFD can be effectively used to examine design parameters and thereby to help improve the design of next-generation multi-rotor drones.

ACKNOWLEDGMENTS

This work was supported by NASA CAS DELIVER project. Terry Parisher and Eric Maglio from Straight Up Imaging provided the CAD model of the SUI Endurance airframe. Eddie Solis scanned both the T-Motor CF blades for the SUI Endurance and Phantom 3 factory rotor blades. Tim Sandstrom made accompanying videos based on the computational work. The first author thanks Carl Russell, Nik Zawodny, Wayne Johnson, Tom Pulliam, Pieter Buning, Neal Chaderjian, Dennis Jespersen, Alan Wray, and Nagi N. Mansour for helpful discussions.

REFERENCES

[1]Young, L. A., "Conceptual Design Aspects of Three General Sub-Classes of Multi-Rotor Configurations: Distributed, Modular, and Heterogeneous," The 6th AHS Specialists Meeting on Unmanned Rotorcraft Systems, Scottsdale, Arizona, Jan. 2015.

[2]Yoon, S., Chan, W. M., and Pulliam, T. H., "Computations of Torque-Balanced Coaxial Rotor Flows," AIAA Paper 2017-0052, The 55th AIAA Aerospace Sciences Meeting, Gaylord, Texas, Jan. 2017.

[3]Chan, W. M., "The OVERGRID Interface for Computational Simulations on Overset Grids," AIAA Paper 2002-3188, St. Louis, Missouri, June 2002.

[4]Chan, W. M., "Developments in Strategies and Software Tools for Overset Structured Grid Generation and Connectivity," AIAA Paper 2011-3051, Honolulu, Hawaii, June 2011.

[5]Nichols, R., Tramel, R., and Buning, P., "Solver and Turbulence Model Upgrades to OVERFLOW2 for Unsteady and High-Speed Flow Applications," AIAA Paper 2006-2824, June 2006.

[6]Pulliam, T. H., "High Order Accurate Finite-Difference Methods: as seen in OVERFLOW," AIAA Paper 2011-3851, June 2011.

[7]Zawodny, N. S., Boyd, D. D., and Burley, C. L., "Acoustic Characterization and Prediction of Representative, Small-Scale Rotary-Wing Unmanned Aircraft System Components," The 72nd AHS Annual Forum, West Palm Beach, Florida, May 2016.

[8]Russell, C., Jung, J., Willink, G., and Glasner, B., "Wind Tunnel and Hover Performance Test Results for Multicopter UAS Vehicles," The 72nd AHS Annual Forum, West Palm Beach, Florida, May 2016.

[9]Yoon, S., Pulliam, T. H., and Chaderjian, N. M., "Simulations of XV-15 Rotor Flows in Hover Using OVERFLOW," The 5th Decennial AHS Aeromechanics Specialists' Conference, San Francisco, California, Jan. 2014.

[10]Yoon, S., Chaderjian, N. M., Pulliam, T. H., and Holst, T. L., "Effect of Turbulence Modeling on Hovering Rotor Flows," AIAA Paper 2015-2766, The 45th AIAA Fluid Dynamics Conference, Dallas, Texas, June 2015.

[11]Yoon, S., Lee, H. C., and Pulliam, T. H., "Computational Analysis of Multi-Rotor Flows," AIAA Paper 2016-0812, The 54th AIAA Aerospace Sciences Meeting, San Diego, California, Jan. 2016.

[12]Yoon, S. Lee, H. C., and Pulliam, T. H., "Computational Study of Flow Interactions in Coaxial Rotors," The AHS Technical Meeting on Aeromechanics Design for Vertical Lift, San Francisco, California, Jan. 2016.

[13]Jespersen, D., Pulliam, T. H., and Buning, P., "Recent Enhancements to OVERFLOW," AIAA Paper 97-0644, Reno, Nevada, Jan. 1997.

[14]Lakshminarayan, V. K. and Baeder, J. D., "Computational Investigation of Micro Hovering Rotor Aerodynamics," *Journal of the American Helicopter Society*, 55, 022001, 2010.

[15]Spalart, P. R., Jou, W-H., Strelets, M., and Allmaras, S. R., "Comments on the Feasibility of LES for Wings and on a Hybrid RANS/LES Approach," *Advances in DNS/LES,* Greyden Press, 1997, pp. 137-147.

[16]Spalart, P. R. and Allmaras, S. R., "A One-Equation Turbulence Model for Aerodynamic Flows," AIAA Paper 1992-0439, Jan. 1992.

[17]Spalart, P. R., "Strategies for Turbulence Modeling and Simulations," *International Journal of Heat and Fluid Flow*, 21, 2000, pp. 252-263.